

First results of site testing program at Mt. Shatdzhatmaz in 2007 – 2009

V. Kornilov,^{*} N. Shatsky, O. Voziakova, B. Safonov, S. Potanin, M. Kornilov

Sternberg Astronomical Institute, Universitetsky prosp. 13, 119992 Moscow, Russia

Accepted 2010 June 14. Received 2010 June 14; in original form 2010 May 26

ABSTRACT

We present the first results of the site testing performed at Mt. Shatdzhatmaz at Northern Caucasus, where the new Sternberg astronomical institute 2.5-m telescope will be installed. An automatic site monitor instrumentation and functionality are described together with the methods of measurement of the basic astroclimate and weather parameters. The clear night sky time derived on the basis of 2006 – 2009 data amounts to 1340 hours per year.

Principle attention is given to the measurement of the optical turbulence altitude distribution which is the most important characteristic affecting optical telescopes performance. For the period from November 2007 to October 2009 more than 85 000 turbulence profiles were collected using the combined MASS/DIMM instrument. The statistical properties of turbulent atmosphere above the summit are derived and the median values for seeing $\beta_0 = 0.93$ arcsec and free-atmosphere seeing $\beta_{free} = 0.51$ arcsec are determined. Together with the estimations of isoplanatic angle $\theta_0 = 2.07$ arcsec and time constant $\tau_0 = 2.58$ ms, these are the first representative results obtained for Russian sites which are necessary for development of modern astronomical observation techniques like adaptive optics.

Key words: site testing – atmospheric effects – techniques: miscellaneous

1 INTRODUCTION

Nearly twenty years passed since astronomers recognized that the progress in ground-based optical observations fully depends on the success in minimization of the destructive influence of atmosphere. Indeed, the new generation telescopes have reached maximal technology-limited sizes and diffraction-limited optical quality and the detectors used have attained nearly 100 percent quantum efficiency. The telescope performance was determined then by the last parameter in the Bowen (1964) formula – the seeing.

The capabilities of a large telescope may be significantly boosted by the use of adaptive optical systems (AO). Meanwhile, knowledge of solely seeing statistics is insufficient for assessment of the AO perspectives at the given site. The design of AO (see Vernin et al. 1991; Roddier 1999; Wilson et al. 2003; Fuensalida et al. 2004; Tokovinin, Baumont & Vasquez 2003) demands the information on the altitude distribution of *optical turbulence* (OT). This need intensified site testing studies about 15 years ago aimed to collect reliable and statistically significant data on OT both in perspective sites (Schoeck et al. 2009; Vernin, Muñoz-Tuñón & Sarazin

2008; Saunders et al. 2009) and at existing observatories (Tokovinin et al. 2003; Thomsen, Britton & Pickles 2007; Wilson, Butterley & Sarazin 2009).

The site selection for the new 2.5-m telescope of Sternberg astronomical institute (SAI, Moscow University) has revealed absence of a reliable and contemporary information on the astroclimate of Caucasian region of Russia. Due to this reason the Shatdzhatmaz summit site near the Kislovodsk city was chosen on the basis of sparse results obtained 40 – 50 years ago and secondary factors.

The night-time astroclimatic characteristics of this place were measured in the end of 1950-s with a star trails photographic technique (Darchiya, Schmeel & Darchiya 1960; Boshnjakovitch et al. 1962) which was standard for that time. Authors demonstrated the site advantage over the lower elevation places. Meanwhile, they clearly realised that the average amplitude of stellar image motion $\sigma \sim 0.3$ arcsec at zenith related only indirectly to the long exposure image quality.

Such situation has forced us to study the site characteristics with an aim to optimise future observations at the telescope which will be installed there.

The modern way to measure OT is based on the theory of wave propagation through inhomogeneous medium and is focused on determination of the refraction index structural

^{*} E-mail: victor@sai.msu.ru

constant C_n^2 . In typical conditions of night time astronomical observations one can make use of the linear weak perturbations approximation where an atmospheric layer produces the wavefront distortion independently from other layers (Tatarskii 1967; Roddier 1981). This simplification becomes invalid only in unusually strong OT conditions. The applicability of the Kolmogorov model of OT on scales 0.01 – 3 meters is also verified many times, while in the 3 – 30 m domain the von Karman model is normally preferred (Tokovinin, Sarazin & Smette 2007).

A number of methods to measure the altitude C_n^2 distribution like SCIDAR (Fuchs, Tallon & Vernin 1998), SLODAR (Wilson 2002), LOLAS (Avila et al. 2008), LUSCI (Tokovinin et al. 2010) was developed which are suited for particular measurement ranges. Meanwhile, the most representative and homogeneous OT data series were accumulated with the DIMM (Sarazin & Roddier 1990) and MASS (Kornilov et al. 2003) techniques for which one can mention the large-scale site selection programs of the 30-m TMT (Schoeck et al. 2009) and 42-m E-ELT ESO (Vernin et al. 2008) telescopes.

We formulated the main goal of our study as the collection of statistically reliable data on seeing and altitude OT distribution during a 2 – 3 years campaign. In parallel, the representative information on the amount and quality of clear night sky, on atmospheric transparency, sky background brightness and on-site weather parameters had to be accumulated.

In the current paper we describe the developed instrumentation and the results of two-years site monitoring. The detailed data analysis and discussion of the results will be presented later. The next two sections provide a general description of the site selected to build the observatory, followed by the automatic site monitor composition. Section 4 presents the two-year statistics of main weather parameters: temperature, wind speed and direction and clear sky data. Afterwards we remind the basics of the MASS and DIMM methods and describe some details of their implementation.

Section 6 is dedicated to the observation procedure and describes the measurement campaign performed at Mt. Shatdzhatmaz. After this we list some data reduction features and particularities. The last section summarises the main OT measurement results and compares them to characteristics of other observatories. Finally the concluding remarks and perspectives are given.

2 GENERAL SITE DESCRIPTION

The place to install the 2.5-m telescope is selected near the 2127 m top of Mt. Shatdzhatmaz (Karachay-Cherkess Republic of Russia, 20 km southward from Kislovodsk), approximately 700 m to south-east from the Highland astronomical (solar) station of Pulkovo observatory (GAS GAO). The mountain belongs to the Skalistiy ('Rocky') ridge which is parallel to the Main Caucasus ridge ~50 km away. Gradually increasing its height, the Skalistiy ridge approaches Mt. Bermamyt with a 2642 m summit some 20 km to west from our site. In the opposite (SE) direction the ridge declines but has a prominent side extension in the form of a high plateau with the 2880 m Western Kinzhal top, 18 km apart from the selected site.

This relief makes the western and northern winds blowing along more or less flat surface while south-eastern winds cross the deep (some hundreds meters) valley of the Hasaut river on the way from Kinzhal to Shatdzhatmaz. These circumstances influence significantly the local climate and atmospheric turbulence characteristics which was also noticed by Gnevysheva (1991).

The 2.5-m telescope tower will be erected some 40 meters from the steep SE slope of the mountain (+43°44'10"N, +42°40'03"E), at elevation 2112 m from the sea level (Fig. 1). Smaller instruments are planned along the ridge to NE from the 2.5-m telescope tower. The light pollution situation is moderately good: the southern horizon is free from significant sources while there is a glow from towns of Caucasus Mineral Waters region at the northern side. The road Kislovodsk – Dzhily Su (northern Elbrus) is going half a kilometre to east from the observatory.

Some 100 km to the west, at northern spurs of the Main ridge, there is Special astrophysical observatory of the Russian Academy of Sciences (SAO RAS), while the Terskol observatory of the Institute of astronomy of RAS is located 50 km to the south. Unlike the selected site, both observatories are situated close to higher peaks.

Climatic parameters of our site are derived from the data of the meteorological station 'Shatdzhatmaz' located 600 m northward of the 2.5-m telescope tower. The year-averaged temperature equals to +2.3°C, the day-time average temperatures vary from -6° in winter to +12° in summer. The mild local climate makes temperatures below -15° and above +20° very rare. The Caucasian humidity is more pronounced in summer (average RH is 80 – 85 percent), while in winter the weather is frequently dry (~ 65 percent). Ground wind is breezy as a rule, although storms exceeding 35 m s⁻¹ do happen from time to time. The surface is alpine meadows covered with non-deep snow in winter which provides the low temperature contrast between days and nights. The weather parameters which we collected at the summit (Section 4) are in agreement with these statistics.

3 AUTOMATIC SITE MONITOR

It is well understood that statistically reliable data on OT and other site characteristics are only obtained in course of regular observations during a long (minimum 2 – 3 years) time span. An optimal solution of this task is to install an automatic site testing monitor functioning with no regular operator intervention. The need of such a robotic facility is supported by both our own experience at Mt. Maidanak (Kornilov et al. 2009) in Uzbekistan and our colleagues' practice.

As a first step, we have developed the suite of automated instrumentation and software for measurement and accumulation of statistics on seeing, altitude OT distribution, clear sky periods, atmospheric transparency and minimal weather parameters (speed and direction of ground wind, temperature and relative humidity). In this development we benefited from experience of similar studies at Cerro Tololo, La Silla, Cerro Paranal and other summits of Chile (Tokovinin, Baumont & Vasquez 2003; Riddle, Schoeck & Skidmore 2006; Schoeck et al. 2009).



Figure 1. Left: the map of the local relief (sides are ca. 2 by 2.5 km). 1 – automatic site monitor of SAI, 2 – 2.5-m telescope mark, 3 – Mt. Shatdzhatzmaz top, 4 – solar station GAS GAO. Right: the view of the automatic site monitor facility at Mt. Shatdzhatzmaz from the South–West with a lab car to the left.

3.1 Equipment

The automatic site monitor (ASM) of SAI was installed at Mt. Shatdzhatzmaz in summer 2007, 40 m to SW from the spot reserved for the 2.5-m telescope. First remote seeing measurements were conducted in October 2007.

The heart of the monitor is the combined MASS/DIMM instrument attached to the automated amateur-class 12-inch telescope Meade RCX400. The telescope and instrument are run by a dedicated computer. This equipment is powered only during observations to assure the detector safety and to minimise power consumption.

The telescope is mounted on a concrete 5-m high pillar having a 0.5×0.5 m section, thus its tube is at 6-m elevation above the ground. Such a height is typical for DIMM facilities at observatories; the 2.5-m telescope primary mirror will also have similar elevation.

The telescope is protected by a custom made enclosure with wooden side walls to minimize thermal effects (Fig. 1). The roof (dome) of the enclosure is constituted by steel arches with a tough waterproof fabric pooled on which are moved by a couple of electric actuators. When fully opened, the enclosure allows to reach stars with zenith distances up to 65° . The enclosure is mounted on the metallic tower composed of three triangles made of 80 mm pipes which are fixed in 3 individual concrete foundations. Such a rigid construction vibrates quite moderately even at winds exceeding 20 m s^{-1} . The observation floor is accessed using a lightweight removable ladder.

Apart from the described OT measurement equipment, there is another compact computer located in the enclosure. It runs days and nights and handles the dome operations, the Wi-Fi link (IEEE 802.11b) with a router at the solar station, the equipment power management and collection of weather data. Two survey webcams are also driven by this machine in order to control the telescope and outdoors area. Meteorological instruments (an anemometer and T and RH sensors) are fixed at the 5-m height on a special mast atop the lab car roof.

The ASM power is supplied by the storage batteries

with a 400 A-h total capacity. This provides 7 – 10 days of operation as the permanently running part consumes about 20 W and the night-time observations equipment needs 40 W in addition.

It should be admitted that technical problems affected our site testing during a rather long period, so completely automatic operation began only in February 2008. The major issues were related to the RCX400 scope which is not very suitable for an autonomous work, having a number of drawbacks and some bugs in its firmware. Also, the batteries charging was problematic until the summer 2008, causing interrupts in the observations.

3.2 Network and software architecture of ASM

In Fig. 2 we illustrate schematically the communication structure of ASM. One can see that it is based on three linked computers controlling the hardware. All computers are running free software under the GNU/Linux OS. Data from the custom-made equipment (MASS instrument electronics, meteo controller, dome and power management units) flow via serial RS485 interfaces¹.

Apart from those described above, there is a computer #3 in the solar station communication room which controls observations and serves as a data storage. Also, it runs an http-server² which allows to control the ASM state via Internet.

The main software consists of a number of independently running applications which communicate with each other via TCP/IP connections. Division of the ASM software into independent components allowed to gain in system flexibility, to maintain the overall system stability and to simplify considerably the logic of each application. The programs are normally running in background as *daemons*.

Each application accomplishes a separate ASM logical task or function. E.g. the TLSP program provides telescope

¹ http://curl.sai.msu.ru/mass/download/doc/new_details.pdf

² URL of ASM server: <http://eagle.sai.msu.ru>

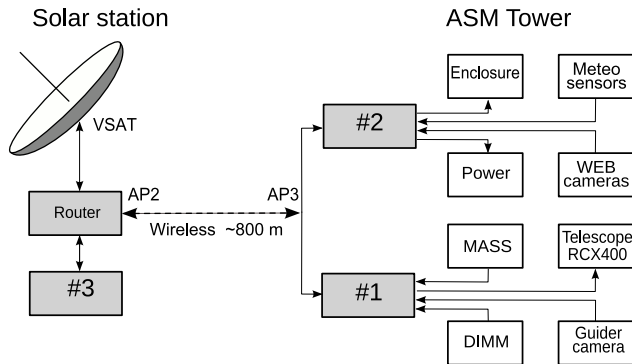


Figure 2. The network ASM structure. #1 – OT measurements computer, #2 – infrastructure control and meteo data acquisition computer, #3 – observation management, data storage and http-server

pointing, object centring and guiding during measurements for which it communicates with the scope and a finder camera.

The programs are all running as servers, processing only external command requests. An exception is the weather data collecting program MONITOR which starts to poll the meteo controller and to store the results in an output file immediately after start-up. Meanwhile, it also provides the server functions, giving the information on actual conditions when requested.

A simple protocol was implemented³ for inter-program communication. The commands are given in text (ASCII) form which also allows to manually operate the program components using a system *telnet* utility while debugging or troubleshooting.

In the automatic mode of operation, the programs are controlled by the supervising program AMEBA running on the computer #3 which generates client requests to the programs. It provides logic of the ASM operation according to the algorithms detailed in Section 6.

4 WEATHER PARAMETERS AND CLEAR SKY STATISTICS

A minimal set of meteo sensors was included in ASM in order to a) provide safe autonomous operation and b) accumulate a homogeneous data set on weather conditions which is also useful for a subsequent analysis of OT monitoring results. No attempt to strictly standardise (calibrate) the measurements was performed. The T, RH and wind sensors are readout by the MONITOR program with a 2-s sampling time to provide instantaneous values which are on-fly averaged in less noisy 1-minute values.

4.1 Clear night sky

The clear skies were monitored since summer 2006 using the Boltwood clouds sensor⁴ which is connected to a server of the MASTER project (Lipunov et al. 2010) at GAS. This

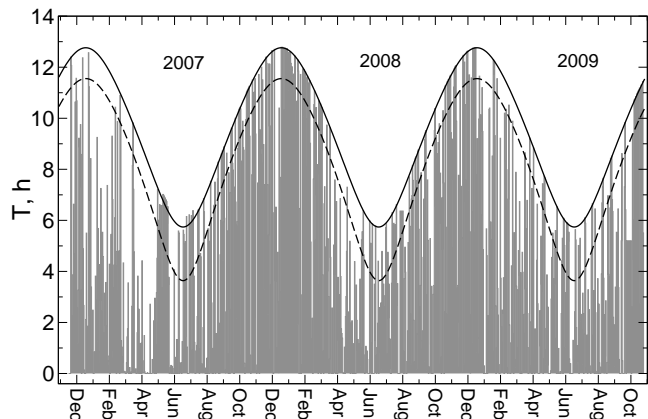


Figure 3. Clear sky nights distribution 2006 November 20 to 2009 October 31. The solid line denotes the nautical night duration, the dashed line does for the astronomical night.

bolometric sensor measures infrared radiation of the sky in spectral range from 5 to 10 μm which gives brightness temperature of the sky. Statistics of clear sky were computed from the 3-years data set spanning the period 2006 November 20 to 2009 October 31. The sky was ranked clear when $\Delta T = T_{sky} - T_{amb} + T_{sen} < -22^\circ\text{C}$ (where T_{sky} , T_{amb} and T_{sen} are temperature readouts from the cloud sensor). This criterion is illustrated by the nautical night time ΔT distribution in Fig. 4 where the left peak reflects the clear sky condition.

Since there are astronomical observations which are not critical to the sky background we expanded the clear sky analysis by two conditions: for astronomical night ($h_\odot < -18^\circ$) and for nautical night ($h_\odot < -12^\circ$). In Fig. 3 the diagram of the clear nautical night sky distribution is shown for the above specified 3-years period.

The annual amount of clear astronomical night sky at Mt. Shatdzhatzmaz is 1343 h, to be compared to the theoretical total 2950 night-time hours at the given latitude. This amount is slightly higher than the Rylkov & Bobylev (1991) estimate of 1200 h. For nautical nights, the annual amount is 1546 h, while the calculated total is 3451 h.

The monthly clear-sky astronomical and nautical time distribution is given in Table 1. It shows that the most favourable observations period is from mid-September to mid-March, containing ≈ 70 percent of the yearly total clear sky hours. This period coincides with the time of the slowest high-altitude wind.

The direct comparison of clear night hours between observatories is complicated by differing clear-sky criteria and the way the data are presented in terms of fraction of the whole night time. However, for Maidanak, La Silla and Paranal observatories the annual clear-sky night time (Table 2) is recalculated from the data of Ehgamberdiev et al. (2000). The estimation of the SAO clear skies is reported by Leushin et al. (1975). We derived the clear sky for peak Terskol using the 0 – 2 cloudiness data from the paper by Depenchuk, Kondratyuk & Kojfman (1977). In the latter study, the authors give the yearly clear sky duration of 1200 h, including partially clear weather.

The ΔT criterion given above is rather strict; it was chosen to avoid frequent ASM shut-downs due to lowering of measured star counts. Such a threshold corresponds rather

³ See http://curl.sai.msu.ru/mass/download/doc/sv_ug.pdf

⁴ <http://www.cyanogen.com/fix.php>

Table 1. Monthly amounts of astronomical and nautical clear night sky CS (in hours) and their fractions of the whole night time (in percent)

Months	Astronomical		Nautical	
	CS	Frac.	CS	Frac.
Jan	158	45	175	46
Feb	131	44	145	46
Mar	85	31	95	31
Apr	45	22	53	21
May	62	40	80	38
Jun	44	39	64	36
Jul	58	42	82	42
Aug	79	40	94	39
Sep	101	41	116	41
Oct	189	62	210	62
Nov	197	60	216	60
Dec	193	54	213	54

Table 2. Annual clear astronomical night sky at six observatories: actual clear sky (in hours), its fraction of the whole night time (in percent) and the whole night time (in hours)

	Clear sky	Fraction	Whole
Shatdzhatmaz	1343	46	2950
SAO	1020	34	2961
Terskol	874	29	2975
Maidanak	1697	55	3088
La Silla	1861	57	3291
Paranal	2604	78	3350

to the conditions which other authors refer to as ‘photometric skies’. Softening the threshold to, say, $\Delta T = -18^\circ\text{C}$ (corresponding to the cloudiness ≈ 25 percent) boosts the clear night fraction from 46 to 58 percent.

4.2 Temperature

The outside temperature sensor is based on the TMP36 circuit (Analog Devices) and is installed in a standard meteorological housing in order to minimize the heating by the sun. The comparison of its reading with data from the cloud sen-

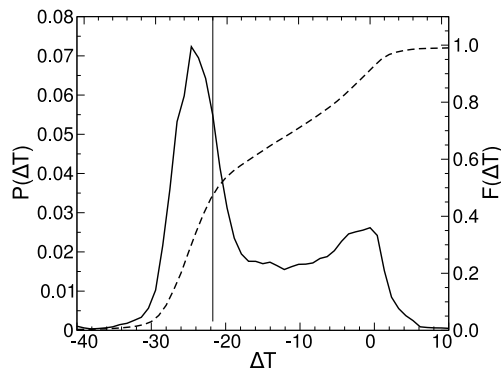


Figure 4. Differential (solid line) and integral (dashed line, right axis) distributions of ΔT in nautical nights. The thin vertical line depicts the selected threshold used for clear sky detection.

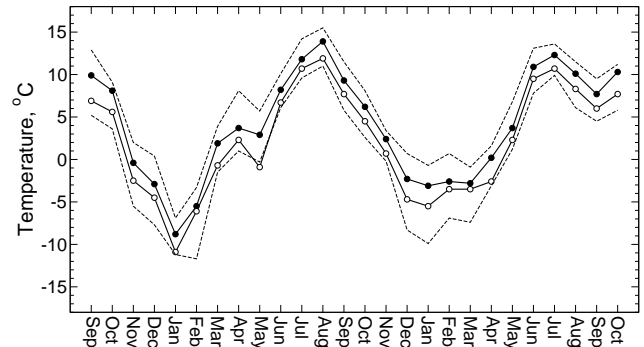


Figure 5. Two-year evolution of the monthly median day-time (black circles) and night-time (open circles) temperatures. Dashed lines trace the first and third quartiles of monthly distributions.

sor and the meteo station records showed the discrepancies to be below $\pm 2^\circ\text{C}$.

Although our weather data accumulation was started on July 19, 2007, the analysis encompasses the period starting from 2007 November 1. The absolute range of temperatures on clear nights is from $+17.8^\circ\text{C}$ to -17.2°C . The median value is $+1.8^\circ\text{C}$ which is more typical for observatories at higher altitudes.

Low temperatures in clear nights reduce the typical precipitable water vapour. Obtained from processing of the GPS signal wet delay data, the water content shows the median value of 7.75 mm. The detailed study on the precipitable water vapour and optical extinction above the summit will be published elsewhere.

As a comparison, the yearly average temperature at SAO which we derived using the weather page data on the observatory website⁵ is $+4.2^\circ\text{C}$ over the same period. When weighted by the observation time distribution, it might be even higher since the summer – autumn is the favoured observing season there. At the Terskol site, the yearly average temperature weighted by observing time is -6.1°C .

In Fig. 5 we present the diagram of night- and day-time temperatures averaged within months. The first and third quartiles Q1 and Q3 of monthly distributions are plotted for reference. It is clear that the two-year data span is not long enough for obtaining statistically reliable monthly averages.

The local turbulence is largely dependent on the contrast between the day- and night-time temperatures. At our site, the diurnal temperature difference is small and amounts to 1.3°C if computed as the difference of temperatures 1 h before and 1 h after sunset. If one takes the full amplitude of daily variation between noon and midnight then it becomes $\approx 3.4^\circ\text{C}$ for those days when the following night was clear.

Similar diurnal temperature variation is observed at SAO RAS where the surface character is similar. At Terskol, the average difference is $\approx 2.9^\circ\text{C}$ as quoted by Depenchuk et al. (1977). These contrasts were computed for the entire data set, without regard to cloudiness.

⁵ <http://www.sao.ru/tb/tcs/meteo/data>

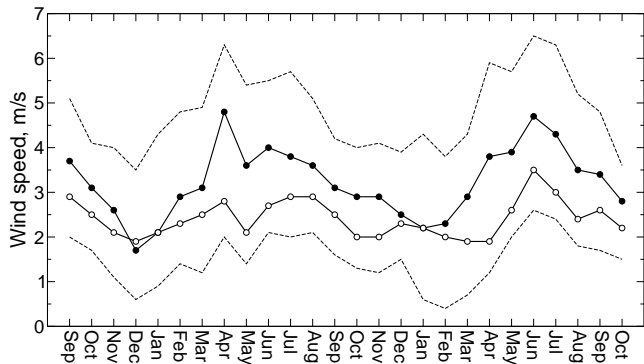


Figure 6. Two-year evolution of the monthly median wind speed during daytime (black circles) and night (open circles). Dashed lines depict the first and third quartiles of monthly distributions.

4.3 Ground wind speed

The strength and direction of ground winds define the air-flow conditions about the local relief and the observatory and influences the generation of the ground-layer turbulence.

Wind speed and direction were measured using a conventional cup anemometer by Davis Instruments (model 7911) attached to the meteo controller. Our data show that the wind at the summit is mostly a light breeze, in agreement with the official meteo statistics. In Fig. 6 the monthly median values of the night- and day-time wind speed are shown accompanied by respective quartiles of the distributions. It is noticeable that the night wind is more stable throughout a year while the daytime wind is stronger in summer.

The global median wind speed is 3.3 m s^{-1} in daytime and 2.3 m s^{-1} at night, both in clear and cloudy time. Similar values are characteristic for the Maidanak summit (Ehgamberdiev et al. 2000) which was distinguished as an advantage over many other observatories. Meanwhile, in 1 percent of cases the wind is stronger than 12 m s^{-1} . In the night time the strong wind is rare; wind speed in excess of 9 m s^{-1} occurs in 2.2 percent of cases. The dependence of wind speed on the time of day is shown in Fig. 7.

The dominant wind direction at night is mostly from the West and, to a smaller extent, from the South-East. The midday behaviour is different, as the NW winds become more frequent. The probability distribution of the wind direction as a function of time of day is shown in Fig. 7 (left). Apparently, preferable wind directions are related to the large-scale relief properties.

The NCEP/NCAR⁶ is a recognized standard source of the high-altitude wind data. According to it, most of the year (October to May) the wind speed at 13 km altitude is about 20 m s^{-1} while in summer (June – September) it increases to 35 m s^{-1} . This can be expected since the Shatdzhatzmaz latitude corresponds to the minimum between the tropical and polar streams. The situation is similar at other moderate-latitude observatories (Carrasco, Avila & Carramiñana 2005).

For comparison, analysis of the weather data at SAO for the 2007 – 2009 period shows the median/mean night-time wind speed to be $2.0/3.8 \text{ m s}^{-1}$ in winter and $1.3/2.3 \text{ m s}^{-1}$

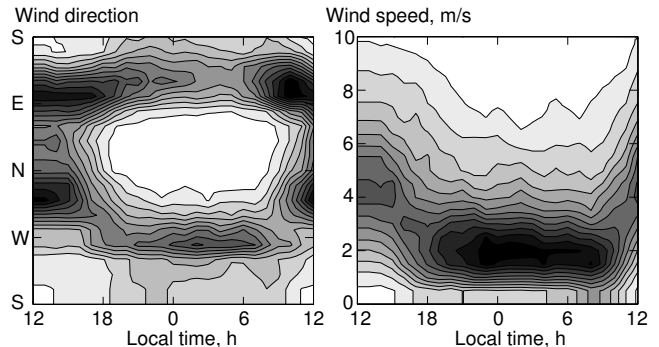


Figure 7. Two-dimensional probability distribution of the direction (left) and strength (right) of wind as function of the local time. Midnight is in the middle, more dense (darker) regions correspond to higher probability.

in summer. Meanwhile, the probability of strong ($>9 \text{ m s}^{-1}$) wind is 0.13 and 0.04, respectively. Nelyubin & Vasilyev (1969) report slightly different situation with 5.9 m s^{-1} in October – March and 2.5 m s^{-1} in April – September recorded in the 1960-s. Similarly to SAO, the winds at peak Terskol are stronger in winter than in summer: $2.5 - 3.6 \text{ m s}^{-1}$ and $1.4 - 2.6 \text{ m s}^{-1}$, respectively.

5 OPTICAL TURBULENCE MEASUREMENT

5.1 The principles of MASS and DIMM instruments

Let us recall that the OT power is described by a single parameter in the Kolmogorov model. This is normally the Fried radius r_0 (atmospheric coherence radius). Meanwhile, a more appropriate measure for description of the turbulence distribution along the line of sight is the turbulence intensity J (having the dimension of $\text{m}^{1/3}$) which is defined as

$$J = \int C_n^2(z) dz, \quad (1)$$

where the integration is performed along the whole light path. J is related to the Fried radius as:

$$J = 0.06 \lambda^2 r_0^{-5/3} \quad \text{or} \quad (2)$$

$$J = 1.5 \cdot 10^{-14} r_0^{-5/3}, \quad \text{if } \lambda = 500 \text{ nm} \quad (3)$$

Unlike other parameters, J is additive and does not depend on wavelength. In order to compare the measurements performed at different air masses M , one should reduce the measured J' to zenith, where the light propagation distance z is replaced by height h : $J = J'/M$.

It is more common to quantify the full turbulence at a given site by the image quality β (seeing) which has a sense of a characteristic size of the turbulent disc (full width at half maximum – FWHM) registered with a long exposure in a large ideal telescope. For $\lambda = 500 \text{ nm}$ this measure (in arcseconds) is

$$\beta = 2 \cdot 10^7 J^{3/5} \quad (4)$$

The theory of the DIMM instrument (Differential Image Motion Monitor) is described by Sarazin & Roddier (1990)

⁶ <http://www.esrl.noaa.gov/psd/data/reanalysis/reanalysis.shtml>

and Tokovinin (2002a). The principle is based on measurement of differential displacement of two star images constructed by two circular apertures. These apertures have the diameter D about 10 cm each and are separated by the baseline distance d about 20 cm in the telescope entrance pupil plane. The star images are offset from each other by additional optical elements.

Such a differential motion is described in terms of differential *slopes* of respective wavefront regions, related to the OT power. The variance of the longitudinal differential motion σ_l^2 (along the apertures baseline) and of the transversal motion σ_t^2 (perpendicular to the baseline) is expressed as

$$\sigma_{l,t}^2 = 16.7 \cdot K_{l,t} D^{-1/3} J. \quad (5)$$

The equation (5) is obtained from a conventional expression from above cited papers by the substitution of r_0 from the formula (3).

For the Kolmogorov's turbulence spectrum, the coefficients $K_{l,t}$ depend solely on the apertures geometry (Sarazin & Roddier 1990):

$$\begin{aligned} K_l &= 0.358 (1 - 0.541 (d/D)^{-1/3}) \\ K_t &= 0.358 (1 - 0.811 (d/D)^{-1/3}). \end{aligned} \quad (6)$$

Thus the DIMM sensor allows to measure the full OT intensity from the telescope entrance to the upper boundary of the atmosphere. This is an essential but still insufficient information.

Multi Aperture Scintillation Sensor (MASS, Kornilov et al. 2003) is a technique allowing to obtain the detailed information on the OT *vertical distribution*. This method is based on simultaneous measurements of stellar scintillation in four concentric entrance apertures. This allows to obtain 4 normal and 6 differential scintillation indices s^2 which are the variances of relative light intensity fluctuations. Scintillation is measured with 1-ms exposure and s^2 are computed for 1-s time intervals (Kornilov et al. 2003; Tokovinin et al. 2003, hereafter TKSV).

The weak perturbation theory implies that scintillation indices s^2 are produced by the whole atmosphere in the following way:

$$s^2 = \int_0^\infty C_n^2(z) Q(z) dz, \quad (7)$$

where $Q(z)$ is a weighting function depending on the wave propagation geometry: the entrance apertures dimensions and angular size of a source. For the particular instrument geometry and assumed spatial spectrum of scintillation the weighting function can be computed theoretically (Tokovinin 2002b; TKSV).

Having 10 equations like (7) with different weighting functions, one can solve the inverse problem and obtain the OT profile from the measured indices s^2 . For a feasible set of entrance apertures (defining the respective set of $Q(z)$) the problem is ill-conditioned so the non-trivial procedure of the vertical profile restoration constitutes a key part of the MASS technique (TKSV; Kornilov & Kornilov 2010). The main drawback of the scintillation method is its blindness to the ground layer turbulence, so without additional measurements in this important domain the results can suffer from considerable incompleteness.

5.2 The combined MASS/DIMM instrument

Since the MASS apertures can be inscribed in a ~ 10 cm circle, both MASS and DIMM methods may be implemented in a single instrument fed by a 10 – 12-inch sized telescope. This was realized in late 2003 and the details of the construction of this combined device and its properties are discussed by Kornilov et al. (2007). The advantages of this approach are obvious: one needs a single telescope, a DIMM channel camera serves for centring and guiding of a star, both methods deal with the same volume of turbulent atmosphere so its non-stationary nature does not prevent the joint analysis of data. These devices were involved in a majority of large-scale site testing campaigns of the last years (Schoeck et al. 2009; Vernin et al. 2008).

Our instrument differs by the model of the DIMM channel detector. A high-speed industrial CCD camera EC650 from Prosilica with Firewire interface (IEEE1394) is used. The camera fully complies with the IIDC standard, so the open library LIBDC1394⁷ may be used to program the data exchange under GNU/Linux OS.

Setting the exposure time to 4 ms allows to achieve the image rate of ≈ 200 frames per second in the region-of-interest (ROI) 60×100 pixels – much faster than with other cameras used in DIMMs. Such a frame rate allows to measure the variances $\sigma_{l,t}^2$ with a maximal possible accuracy. The low readout noise of $\approx 10e^-$ allows to use stars up to 4 magnitude.

An important calibration parameter of DIMM is the pixel scale of the detector since $\sigma_{l,t}$ in eq.(5) must be in radians. Initially we estimated the scale in a conventional way with help of the visual double star HR7141/2 = θ Ser having a 22.3 arcsec separation. The diurnal sky rotation appeared to provide us with a more convenient and precise way to calibrate the scale delivering the value 0.612 arcsec per pixel. The entrance aperture dimensions d and D are set by the physical sizes of the DIMM mask which is located in the exit pupil of the 'telescope+instrument' system and by the magnification k of this system. The d/D ratio was measured as 2.18 ± 0.02 , the aperture sizes D were 90 mm both.

The OT profile restoration is based on precise knowledge of weight functions (7) which also depend on the system magnification k determining the effective sizes of entrance apertures. So, each focusing of the Fabry lens was followed by the measurement of k with 1-2 percent precision ($k = 16.3$ in the final state). Since functions $Q(z)$ involve also chromatic effects and thus depend on the spectral response of MASS detectors, the latter was controlled⁸ by special observations of stars with a wide range of colours similarly to the technique of Kornilov et al. (2009).

The MASS channel data reduction requires also other instrumental parameters, namely the detectors non-poissonity p and non-linearity τ which serve to correct exactly for the photon-noise contribution to measured variances (Kornilov et al. 2003). These parameters were also monitored using dedicated measurements.

⁷ <http://damien.douxchamps.net/ieee1394/libdc1394/>

⁸ http://curl.sai.msu.ru/mass/download/doc/mass_spectral_band_eng.pdf

5.3 MASS/DIMM control and data acquisition

Unlike the service applications described in Section 3.2, the MASS/DIMM driving programs MASS and DIMM affect not only the overall ASM efficiency but the reliability of the results themselves.

The principal functionalities of the MASS program are practically the same as those of preceding TURBINA program and are described in (TKSV; Kornilov et al. 2007). The main difference is the absence of graphical user interface and real-time profiles restoration which proved to be a source of instability in automatic and remote mode of operation.

The program performs continuous light intensity recording in A, B, C and D apertures with elementary integration time of 1 ms during 1-s basic measurement. This data set is on-line processed in order to compute different statistics: variances and covariances with time lag 1 and 2 for normalized signals and their combinations. These statistics are stored in the output file for subsequent processing.

Measurements are started by an external command and repeated over an accumulation time. The mentioned integration, basic and accumulation times along with other parameters specifying the measurement process are read by the program from a configuration file during initialization. No command can change these settings which ensures the good homogeneity of output results.

The DIMM program for communication with the DIMM-channel camera has a similar functional structure. Each sub-frame obtained from the video stream (containing the image of the ROI) is processed to recognize two stellar images for which the gravity centres and other characteristics are computed. The frame exposure, measurement time and accumulation time are also defined by a configuration file.

A special command initiates the measurement of the star position in a full frame when searching for the new target and starting guiding.

6 OBSERVING CAMPAIGN

6.1 The RCX400 telescope peculiarities

Remote and automatic observations demand pointing accuracy of about 1 arcmin in order to get a target well inside the MASS/DIMM field diaphragm having a ≈ 2 arcmin radius. Such an accuracy is achievable with RCX400 after one determines the telescope coordinate system using the 3-stars method. Meanwhile, bugs in the instrument firmware cause the telescope controller to occasionally lose this reference, while its remote recovery does not provide the needed precision.

To cope with this situation, we attached a web camera (Philips SPC900NC) to the telescope finder which allows to detect stars up to 8 magnitude in the $0.9^\circ \times 1.2^\circ$ field of view. The TLSP program uses images from that camera to search, centre and guide targets. But the accurate guiding during OT measurements is made using the DIMM channel information.

Introduction of a CCD-finder and development of optimized procedures to restore the telescope coordinate system after powering it on and to explicitly control the axes movement while slewing solved the pointing problem. More than

3500 successful pointings were performed during the campaign.

Another major RCX400 problem is its focusing which gradually deteriorates the optical adjustment (so-called collimation). The accumulating tilt errors of the secondary mirror produce coma which is seen as astigmatism in the DIMM apertures, biasing measurements of OT strength (Tokovinin & Kornilov 2007). Meanwhile, the documented collimation procedure can only be performed interactively. Only in the autumn 2009 we overcame this restriction⁹.

In general, the ‘telescope+DIMM’ optical system was maintained in a good state. The quality was controlled by the Strehl ratio S of the DIMM images; its median value over the whole campaign was 0.47 for both apertures¹⁰. Only in the period from April to June 2009 the telescope alignment was worse and S progressively decreased to 0.3 (left image) and 0.2 (right image). At most 5 percent of measurements were performed in this state.

Another annoyance was dew condensation on the telescope corrector plate in windy and humid conditions. Invention of a special-shape dew cap in November 2007 allowed us to get rid of this problem.

An additional factor limiting the measurement ability is a wind-caused telescope vibration. In slow wind conditions the common image motion is about ± 0.5 arcsec and is mainly caused by cophased turbulence effects and telescope tracking errors. With the wind speed in excess of 3 m s^{-1} the vibration amplitude grows almost linearly and approaches 10 arcsec in elevation when the wind is $7 - 8 \text{ m s}^{-1}$. The amplitude in azimuth is two times less. The wind gusts excite several telescope eigenmodes near 10 Hz, so the vibration amplitude may exceed eventually 20 arcsec. In this case the ROI must be enlarged and the framerate becomes slower.

More importantly, in these conditions the images are moving so quickly ($>600 \text{ arcsec s}^{-1}$) that the respective smearing exceeds 2.4 arcsec during exposure. As in the optical aberrations case, this effect introduces DIMM measurement errors and biases the OT estimations up for strong high turbulence. Luckily, 97 percent of measurements were made with vibration amplitudes below 6.4 arcsec and 85 percent with <3 arcsec.

6.2 Operation control and time coverage

Control of the ASM is performed by the AMEBA program which is started daily in the evening at the computer #3 and communicates with respective servers.

OT measurement is initiated when the following conditions are fulfilled: 1) the sun altitude is below -12° ; 2) the cloud sensor reports clear sky; 3) the wind speed does not exceed some limit; 4) the battery voltage is normal. Humidity was not decisive because of the odd sensor behaviour near the dew point, when condensing moisture induced an abrupt lowering of the sensor reading.

When all conditions are satisfied, an observation session is started consisting of the following stages:

- (i) Dome opening, powering up the observation equipment, TLSP, DIMM and MASS programs initiation.

⁹ See http://curl.sai.msu.ru/mass/download/doc/rcx_advices.pdf

¹⁰ http://curl.sai.msu.ru/mass/download/doc/shtrel_controls.pdf

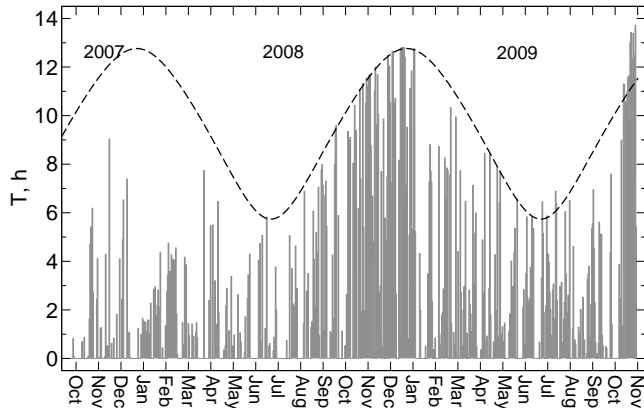


Figure 8. Duration of measurement plotted for the whole period of ASM monitoring. Dashed line is the nautical night duration ($h_{\odot} < -12^{\circ}$).

(ii) Target selection from a list¹¹ of 119 bright stars according to its magnitude, altitude, distance to the Moon and available measurement duration.

(iii) Pointing to the target followed by its search, centring, brightness check and guiding start-up.

(iv) Background measurement in the MASS channel is performed before and after target measurements.

(v) In the case of the failed pointing or high background, another target is selected.

(vi) The target measurement session is performed during 1.5 hours or until one of the selection criteria is violated.

(vii) In the case of an error during measurement (equipment failure, stellar flux drop) another target is selected.

(viii) If an error occurs three times in row, the session is finished; the dome is closed and the equipment is switched off.

After the session is finished by worsened conditions, AMEBA waits for their restoration. In order to prevent random effects, the hysteresis is introduced. For example, observations stopped by the wind speed in excess of 9 m s^{-1} will be resumed after the wind speed remains below 6 m s^{-1} during 20 minutes. Such a pause is obligatory after any session is stopped by an error. Note that the system initialization and parking lasts 2 – 3 minutes. At the end of the night, AMEBA stops conditions checking or a measurement session and shuts itself down.

In the course of a few months after the campaign beginning we have been operating ASM remotely while simultaneously developing and testing the automatic operation algorithms. This period supplements 10 percent of the data. Fully automated observations were started in February 2008.

In Fig. 8 the duration of nightly measurement sessions is plotted for every calendar date of the whole campaign. The total observation duration defined as the sum of time spans between the dome was opened and closed is 1753 h. The net measurement time is 1485 h or $\approx 90\,000$ OT determinations, while about 18 percent of time was spent for service operations: pointing, centring, background measurements etc. In October 2009 the observation sessions lasted

Table 3. Monthly duration of measurements in nights (n) and hours (h) in 2007 – 2009. Efficiency (E) is given in percent.

Year	2007			2008			2009		
Month	n	h	E	n	h	E	n	h	E
Jan	–	–	–	19	36	12	14	63	44
Feb	–	–	–	21	57	26	17	83	79
Mar	–	–	–	11	24	18	19	60	63
Apr	–	–	–	14	31	48	19	65	82
May	–	–	–	10	20	39	15	40	63
Jun	–	–	–	13	33	54	18	64	83
Jul	–	–	–	10	23	30	22	68	92
Aug	–	–	–	20	75	72	20	47	48
Sep	1	1	1	15	64	58	15	40	52
Oct	10	29	13	23	174	85	18	192	97
Nov	11	24	11	24	187	85	–	–	–
Dec	13	30	13	27	220	88	–	–	–

longer than nautical nights since experimental twilight observations were introduced.

In Table 3 we list the total monthly measurement duration for the whole period of the campaign. One should beware that nights were accounted as observational when even a single successful OT measurement was performed.

The E column reflects the efficiency of the clear time use and characterizes the gradual decrease of technical problems. The global efficiency for the whole period is 0.49.

7 OT MEASUREMENT DATA REDUCTION

7.1 Features of reduction and its modifications

The conventional DIMM data processing is quite simple: turbulence intensity J is computed directly using eq. (5) after longitudinal and transversal variances are converted from pixels to radians. Then J is reduced to zenith and expressed as seeing β if necessary.

Meanwhile, there is a number of features which upset this simplicity. The first is a finite exposure which suppresses the high-frequency part of the differential image motion. This effect becomes apparent in strong wind in the boundary layer, where the main part of turbulence is usually located, and at high altitudes with wind streams of $25 - 40 \text{ m s}^{-1}$. It is common to use a double exposure method when frames of single and double exposures are interlaced and a certain extrapolation (Tokovinin 2002a) is exploited to get a ‘zero-exposure’ variance estimation based on theoretical considerations (Martin 1987; Soules et al. 1996).

The use of high-speed cameras does not allow for this technique since exposure cannot be changed without stopping the video stream. Instead, the DIMM program calculates the covariance coefficient between the image coordinates in adjacent frames. Such an approach is theoretically justified by V. Kornilov & B. Safonov¹². Since exposure is as low as 4 ms the correction does not exceed 0.05 for 90 percent of measurements.

A complementary feature is related to the low-frequency domain of the image motion power spectrum. In order to

¹¹ http://curl.sai.msu.ru/mass/download/doc/new_mass_cat.pdf

¹² http://curl.sai.msu.ru/mass/download/doc/dimm_specs.pdf

make possible the joint analysis of MASS and DIMM data aimed to restore the full OT profile, the DIMM measurement *basetime* has to be 1 or 2 s. In this case, part of the power produced by slowly drifting air in the ground layer escapes detection in the DIMM channel.

The low-frequency power is estimated using the variance of basetime-derived images separations computed over the *accumtime* span (covering normally 60 s) and this power is added to the basetime-derived results. This allows to find a trade-off between statistically reliable accumulation time and process stationarity period and to ensure that the method detects a large fraction (> 0.99) of the motion power.

The third circumstance is that equation (5) is valid only in the near-field approximation i.e. when $D^2 \gg z\lambda$. This condition is not fulfilled in practice and thus not all the high-altitude turbulence is measured due to wave propagation. This effect was evaluated (Tokovinin 2002a; Tokovinin & Kornilov 2007), but was ignored in practice because its correction implies the knowledge of OT distribution.

The MASS data processing is based on the solution of an equation set of the kind (7) for a fixed altitude grid under restriction that the solution must be non-negative. This restriction regularises the solution. The technique of the OT vertical profile restoration from scintillation indices and its features were described by Kornilov et al. (2007) and TKS_V.

Experience gained in previous MASS data processing allowed us to significantly modify the algorithms and structure of the data processing utility ATMOS which initially was part of the TURBINA program. The non-linear minimization method was replaced by a much faster and mathematically proven non-negative least squares method (NNLS). Also, the OT profile restoration by *accumtime*-averaged scintillation indices was replaced by averaging the OT profiles restored from the 1-s data. Such an algorithm modification (ATMOS-2.96.0A) reduces the profiles errors and leads to more physically justified turbulence characteristics (Kornilov & Kornilov 2010). Additionally, this permits restoration of an OT profile using denser altitude grid for more accurate localization of the turbulence features. Quality of the profile restoration is controlled by the total residual R^2 which is the *accumtime*-averaged sum of squared residuals of indices.

A further modification (ATMOS-2.96.7) of an algorithm involves the DIMM data in the OT profile restoration. A polychromatic representation of the DIMM weighting function $W_{l,t}(z)$ was deduced by V. Kornilov & B. Safonov¹³ which, analogously to eq. (7), allowed to relate the differential motion variance σ^2 to the refractive index structural coefficient distribution:

$$\sigma_{l,t}^2 = \int_0^\infty C_n^2(z) W_{l,t}(z) dz, \quad (8)$$

The new linear equations system is obtained from the original one for scintillation indices by addition of two equations for longitudinal and transversal components of differential motion and by adding a zero-height point to the altitude grid.

Apart from direct determination of the ground turbulence intensity it is possible now to correct the propagation effect in the differential motion. Non-negativity of the ground layer intensity also stabilizes the solution. A detailed description of the new algorithm and its features will follow.

It is important to note that DIMM weighting functions are calculated under assumption that our DIMM measures differential motion which is better matched by aperture wavefront slope in the Zernike polynomial approximation, namely the so called *z-tilt*, rather than gravity centre displacements (*g-tilt*), according to Tokovinin (2002a). This decreases slightly (by 3 and 5 percent for longitudinal and transversal components, respectively) the derived intensities as compared to those from eqs. (5) and (6).

7.2 Data filtering

The raw MASS data set contains 89189 one-minute star measurements and 6544 background measurements (in 404 nights). When there are DIMM data for the same time intervals they are included in the processing. For some periods they are unavailable, mostly in cases of excessive telescope vibration when a star escapes frequently from the ROI. In this situation no ground layer restoration is performed.

Since the background level is involved in scintillation index computation, it is essential to detect and reject cases when some star was present in the field aperture while the background was recorded. The program accepts the background measurement only if its variance is consistent with solely the photon noise. The target measurements with intensities only marginally exceeding the background level are also rejected.

The data which have passed filtering (88664 meas.) are used in OT profile restoration and integral atmospheric parameters calculation. The residuals analysis is performed to clean out the outlying cases in 1-s OT data set which may affect output statistics.

A further filtration was made while analysing the output results. The events of clouds, the corrector plate fogging, star escapes from the diaphragm, etc. were detected by the D-channel count drop below 100 pulses per ms and by relative flux error exceeding 0.05. The latter value is much more than the median 0.002 of the relative errors due to scintillation, so the derived statistics were not biased. These checks have rejected 0.9 percent of data. Finally, extinction star measurements were thrown away if performed at air mass higher than 1.38. MASS instrumental problems in the period between July 19 and 23 (2008) were detected by abnormal C/D flux ratios.

The residuals analysis has demonstrated that including DIMM data in the profile restoration significantly increases the total residual R^2 (from 1.46 to 2.62 for the global median) in spite of the weak coupling of MASS and DIMM data. The reason was an inconsistency between longitudinal and transversal image-motion variance. When only one DIMM equation is included in the system (either *l* or *t*), the R^2 drops back to almost its original, MASS-only level.

The distribution of residuals is similar to the one without DIMM data but starting at $R^2 \approx 4$ it shows a prominent flat tail. In these cases the actual data come into severe conflict with the model. Their inspection allows to propose two main reasons: 1) sometimes MASS determines stronger

¹³ http://curl.sai.msu.ru/mass/download/doc/dimm_specs.pdf

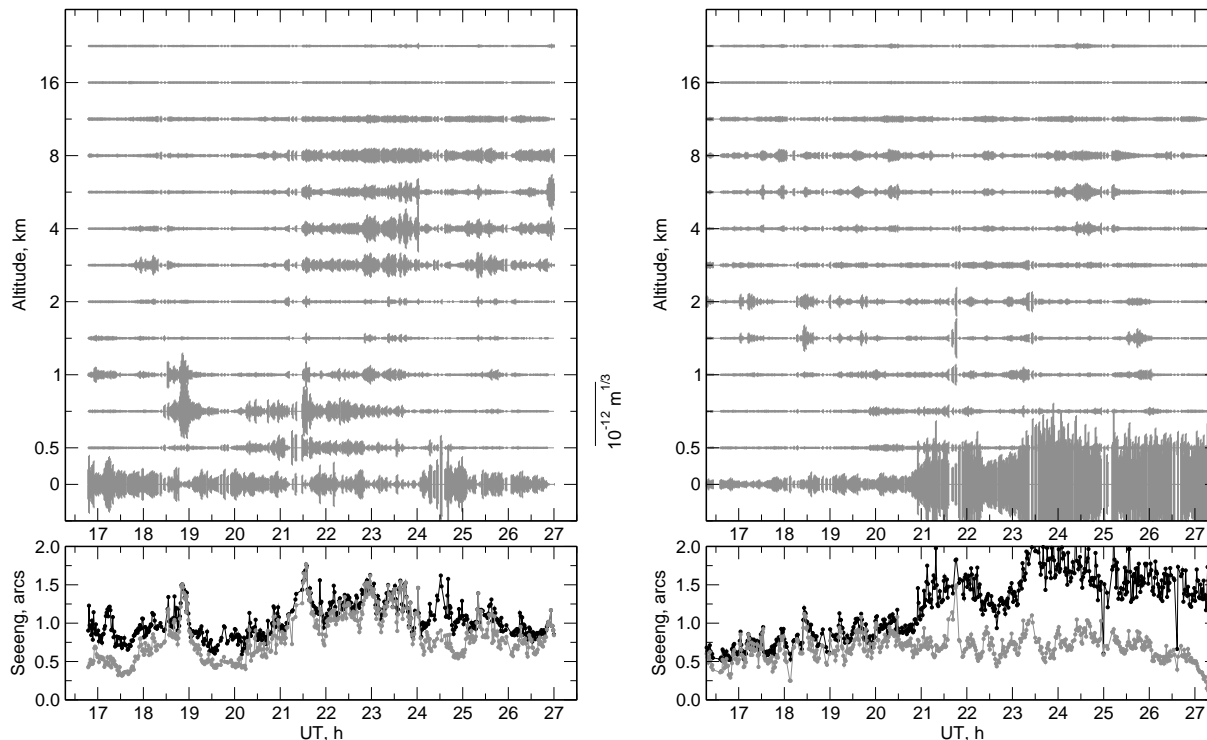


Figure 9. Examples of nightly data processing for 2009 February 19 (left) and 2009 October 24 (right). For each layer, the vertical bars length is proportional to the restored intensity. Scale is shown between the plots. Lower panels – the records of seeing β_0 (whale atmosphere, black points) and of the free atmosphere seeing β_{free} (grey points).

turbulence than follows from the DIMM data, and 2) longitudinal and transverse components of the differential motion are mutually incompatible.

The first situation is discussed in a number of papers as ‘overshoots’ or ‘negative ground layer’ problem and is considered in Section 8.3. Although we made some progress in treatment of those cases (see above) and they are encountered now quite rarely, they have not disappeared completely. The second reason became especially prominent in June 2009 due to optics misalignment when the median residual grew up to ≈ 5 .

To filter out the completely inadequate solutions, we adopted a threshold residual $R^2 = 12.4$ which corresponds to 0.5 percent cases which appear to be indeed marginal. Finally, a total of 85512 OT measurements have passed all filters and are included in the statistics discussed below.

8 TURBULENCE MEASUREMENT RESULTS

8.1 Seeing statistics

Vertical OT distributions were restored on the logarithmic altitude grid of 13 layers at 0, 0.5, 0.71, 1, 1.41, 2, 2.82, 4, 5.66, 8, 11.3, 16 and 22.6 km above the observatory. This grid is based on the conventional MASS grid (see TKS_V) with intermediate and zero-height nodes inserted. As an example, in Fig. 9 we present processing results for two nights which show different OT characters: on February, 19 (2009) the conditions got worse after midnight when turbulence intensified at 3 – 8 km, and on October, 24 it was a ground layer which was responsible for the seeing deterioration. The

wind data for this night report that at 22 h the ground wind became stronger and changed direction.

As previously said, the OT power can be characterised by different measures: intensity J , seeing β , or by the Fried radius r_0 . The processing results are expressed in terms of J but further on we will also use seeing, depending on the context. Quantities related to the whole atmosphere will be referred to as J_{total} and β_0 .

The discussion of OT at a given site and the subsequent use of results involve normally the a distinction between ground and boundary layers. Here we consider layers at 0.5 km and above as free atmosphere. The respective turbulence intensity is denoted J_{free} .

A convenient and common way to present statistics of the OT vertical distribution is a cumulative distribution for the sum OT intensities from a given height h to the upper boundary of the atmosphere. In other words these curves tell us what is the image quality for an observer at a given h . As shown in (Kornilov & Kornilov 2010), these integrals possess a higher precision than intensities in individual layers since errors in adjacent layers anti-correlate.

Such cumulative distributions expressed in terms of seeing are shown in Fig. 10 (top). Their characteristic points are listed in Table 4. The graph at the bottom contains most relevant distributions β_0 and β_{free} . The distribution of β_0 derived from the OT profiles coincides with the one computed by the conventional DIMM formula to within ± 0.01 arcsec. For the free atmosphere, the difference between the OT profile and the integral moment-derived β_{free} is more visible but the median difference is 0.04 arcsec only.

The same plot shows the ‘winter’ (September – Febru-

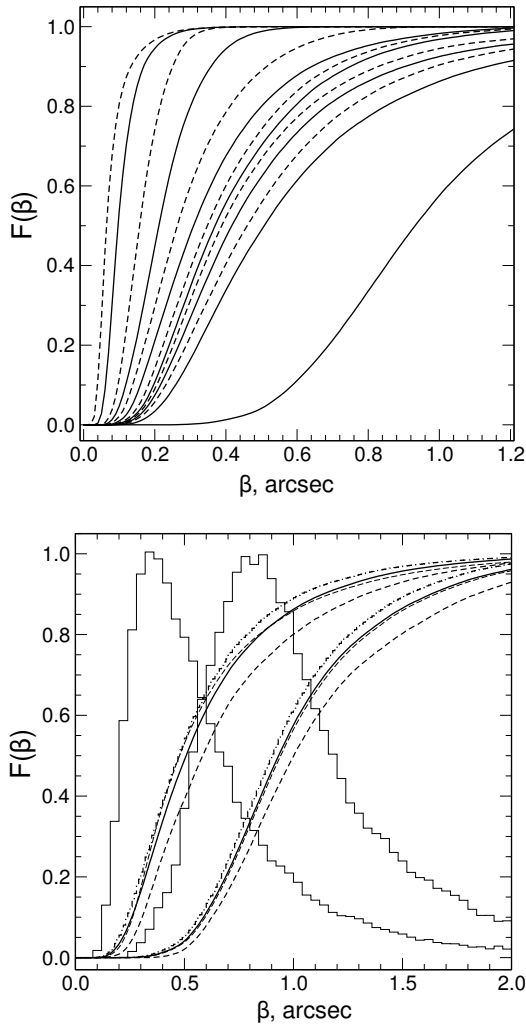


Figure 10. Top: integral distributions of the total OT intensity expressed as seeing β_h computed for atmosphere layers at h and above. Solid lines from right to left: total atmosphere, 0.5 km and higher, 1 km and higher, etc. for 2, 4, 8 and 16 km levels. Dashed lines are the same for intermediate heights. Bottom: integral distributions of the total image quality β_0 (right solid line) for the total data set, for winter (dash-dotted) and summer (dashed) seasons. Thin dashed curve shows the distribution of β_0 computed by the conventional formula. Leftmost solid and thin curves present β_{free} derived from OT profiles and from the zero-order moment (integral atmosphere parameter M_0). Thin step-like curves are differential β_0 and β_{free} distributions.

ary) and ‘summer’ (March – August) seasonal distributions. Since the winter data are 2.4 times more voluminous, the ‘winter’ curve tends to fit the global one, differing by 0.02 arcsec only. The ‘summer’ seeing has a median of 1.00 arcsec.

Differential β_0 and β_{free} distributions allow to determine the *mode* which characterizes the most probable value of seeing at Shatdzhatmaz. Since the curves are positively asymmetric the modes are considerably less than the medians and equal to 0.82 and 0.35 arcsec, respectively.

It should be stressed that integral distributions as well as the dependence of mean or median layer intensity on its altitude are useful for general statistical OT evaluation at a given site. Meanwhile they could hardly help to understand

Table 4. The quartiles of the OT intensity J (Q2 is a median) which is generated by the given altitude layer (in km) and the layers above and of the respective seeing β .

Layer	β''			$J, \times 10^{-14} \text{ m}^{1/3}$		
	Q1	Q2	Q3	Q1	Q2	Q3
Whole	0.731	0.932	1.222	40.3	60.4	94.8
0.5+	0.349	0.508	0.760	11.8	21.9	43.0
0.71+	0.315	0.460	0.680	9.89	18.6	35.7
1.0+	0.291	0.417	0.617	8.68	17.0	30.4
1.41+	0.273	0.388	0.575	7.82	15.8	27.0
2.0+	0.261	0.370	0.542	7.23	14.0	24.5
2.82+	0.243	0.348	0.507	6.41	12.9	21.8
4.0+	0.214	0.309	0.455	5.20	9.58	18.2
5.66+	0.186	0.263	0.375	4.12	7.33	13.3
8.0+	0.157	0.212	0.279	3.10	5.10	8.10
11.3+	0.121	0.157	0.202	2.02	3.11	4.72
16+	0.076	0.097	0.128	0.92	1.38	2.19
22.6	0.049	0.064	0.090	0.45	0.70	1.22

Table 5. Monthly seeing distributions for the whole atmosphere and for layers at 1 km and above (in arcseconds). N is the number of measurements in a given month.

Months	N, 10^3	Total seeing β_0			Free seeing β_1		
		Q1	Q2	Q3	Q1	Q2	Q3
Jan	5.0	0.77	0.98	1.28	0.27	0.42	0.63
Feb	7.8	0.82	1.00	1.28	0.37	0.56	0.87
Mar	3.9	1.30	1.70	2.06	0.55	0.88	1.35
Apr	4.7	0.75	1.02	1.45	0.28	0.39	0.58
May	2.9	0.73	0.95	1.38	0.30	0.39	0.60
Jun	4.3	0.78	0.91	1.10	0.35	0.43	0.54
Jul	3.6	0.80	0.93	1.12	0.38	0.53	0.71
Aug	5.6	0.70	0.95	1.16	0.31	0.46	0.65
Sep	5.3	0.80	0.97	1.21	0.29	0.38	0.55
Oct	18.5	0.64	0.82	1.04	0.23	0.34	0.50
Nov	11.0	0.65	0.84	1.16	0.26	0.36	0.52
Dec	13.0	0.78	0.97	1.25	0.32	0.44	0.61

the atmospheric processes since they do not reflect correlations between turbulent layers.

Of a considerable interest are the seasonal variations of characteristic OT quantities. Although we cover only two years of observations at Shatdzhatmaz and the monthly behaviour isn’t well defined, we may already confidently conclude from Table 5 that October and November deliver the best conditions both in total turbulence and in the free atmosphere. On the other hand, the end of winter (March) shows a remarkably strong turbulence.

8.2 Ground layer properties

Particularly important is the behaviour and characteristics of the ground layer as a dominant contributor of turbulent atmosphere. In principle, simultaneous MASS and DIMM measurements allow to extract its power as a difference of J_{total} and J_{free} values which in fact originate from different instruments and methods. It’s evident that systematic errors of their determination will amplify in a difference $J_{total} - J_{free}$. In cases when the ground layer dominates, this is not

that critical, but when it is weak or when the high-altitude turbulence is strong the problems could arise.

Potential systematic biases of DIMM results are already described and taken into account in the data processing. Meanwhile, the noticed uncertainty in the slope type which is sensed by the particular DIMM instrument is not still experimentally examined. It is probably neither z-tilt nor g-tilt but some intermediate characteristic. The maximum resulting uncertainty is about 17 percent in intensity or 10 percent in seeing.

There are biases in the MASS data processing as well, described in detail by Tokovinin & Kornilov (2007). The most significant is a deviation from the weak-perturbation approximation in the case of strong high turbulence, causing near-saturated scintillation to develop in small apertures. Although authors do provide some empirical correction, the derived solution is formally worse by the R^2 criterium. That's why the ATMOS-2.96 data processor makes only the following corrections of scintillation indices:

$$s^2 = \ln(\bar{s}^2 + 1), \quad (9)$$

where \bar{s}^2 is the computed index in a sense $\langle \delta I^2 \rangle / \langle I \rangle^2$. The reason is that the MASS weighting functions are defined for the $\chi = \ln A$ fluctuations where A is a light wave amplitude and the scintillation index is defined as $s^2 = 4\sigma^2$, where σ^2 is a variance of χ . The measured light intensity has a log-normal distribution and for a strong scintillation ($s^2 \sim 0.5$) this leads to a 20 percent error.

This problem was also discussed in the past but consideration of a nearly saturated scintillation refrained us from additional diminishing of scintillation indices. Nevertheless, the real data examination has shown that the described correction works in the right way: the OT power becomes weaker and the turbulence itself tends to localize higher.

The first estimation of the ground layer intensity \hat{J}_{GL} was obtained from the altitude turbulence moments and the conventional formula (5). Our study reveals that application of the correction (9) decreases the fraction of problematic data from ≈ 0.10 to < 0.04 and such data do not originate from random errors of the ground layer intensity determination.

In Fig. 11 we show the dependence of the median values \hat{J}_{GL} (calculated over groups of 1000 points) on J_{free} . It is clear that in conditions of a very weak (about $4 \cdot 10^{-14} \text{ m}^{1/3}$) free atmosphere OT $\hat{J}_{GL} \approx 2 \cdot 10^{-13} \text{ m}^{1/3}$ (nearly 0.5 arcsec), i.e. it exceeds significantly the J_{free} intensity. As turbulence gets stronger, \hat{J}_{GL} increases. Such a relation indicates a weak and most probably indirect interrelation between GL and free atmosphere. Further, the ground layer intensity stabilizes at the level $4 \cdot 10^{-13} \text{ m}^{1/3}$ (≈ 0.7 arcsec) and remains unchanged while $J_{free} < 1 \cdot 10^{-12} \text{ m}^{1/3}$ (≈ 1.3 arcsec).

The ground layer intensity \check{J}_{GL} derived from the OT profile restoration behaves in a similar way. Meanwhile, when the free atmosphere turbulence becomes too strong and the above-mentioned systematical effects cause the \hat{J}_{GL} to drop tending to negative values, \check{J}_{GL} remains positive.

Such a difference is explained by the propagation effects becoming significant for DIMM measurements in dominant free atmosphere turbulence conditions. An additional circumstance is a non-negativity restrictions applied in OT restoration which act similarly to saturated indices correction, i.e. decreasing and rising the resulting turbulence.

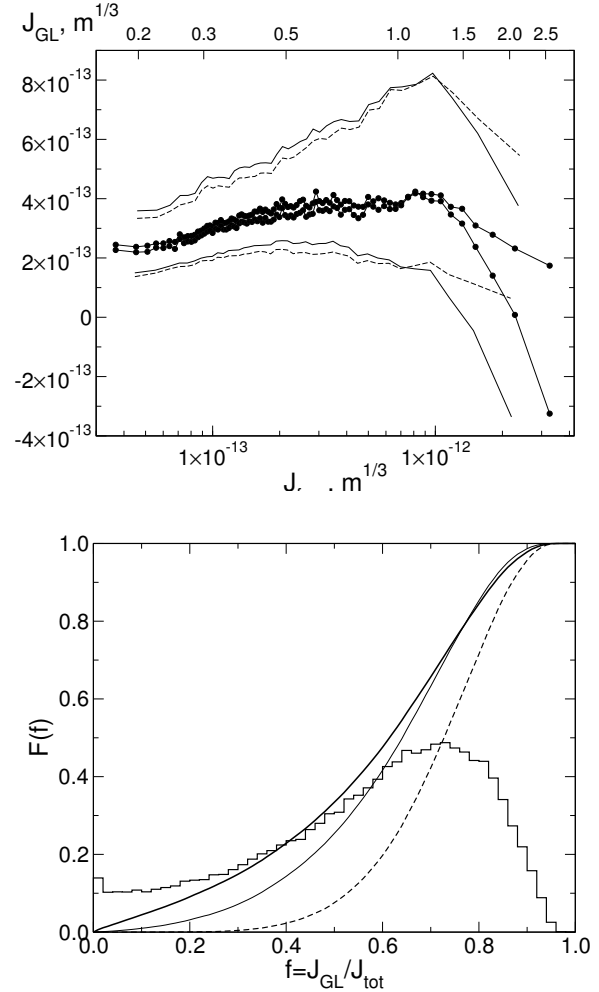


Figure 11. Top: dependence of a median ground layer power as obtained from integrals J_{total} and J_{free} (black dots) and from OT profiles (open circles) on the intensity J_{free} . Thin solid and dashed curves depict first and third quartiles of respective distributions. Bottom: integral distribution of the ground layer intensity fraction for the total data set (thick solid line), the $\beta_0 < 0.93$ arcsec subset (thin solid) and the $\beta_{free} < 0.50$ arcsec subset (dashed). The stair curve is differential total distributions.

In Fig. 11 (bottom) we plot the differential and integral distributions of the fractional power f of the ground layer. The integral distribution of all measurements demonstrates the systematics in the small f domain, with a small excess of zero values. This shows that the implemented correction is not sufficient, although it prevents negative \check{J}_{GL} values.

These effects are diminished in the f distribution for the cases of β_0 better than median and are absent in the $\beta_{free} < 0.50$ arcsec conditions. Note that the distribution is highly asymmetric due to the nature of f being a ratio, so the mode and the median are largely different. For the total data set, the mode and the median are 0.71 and 0.61, for the sample $\beta_0 < 0.93$ arcsec they are 0.71 and 0.64, and when $\beta_{free} < 0.50$ arcsec they are 0.78 and 0.73.

One can expect that a complete correction for saturation would make the total data distribution closer to the good-images case, i.e. the median fraction of the ground layer will increase to ≈ 0.65 . This value is typical for

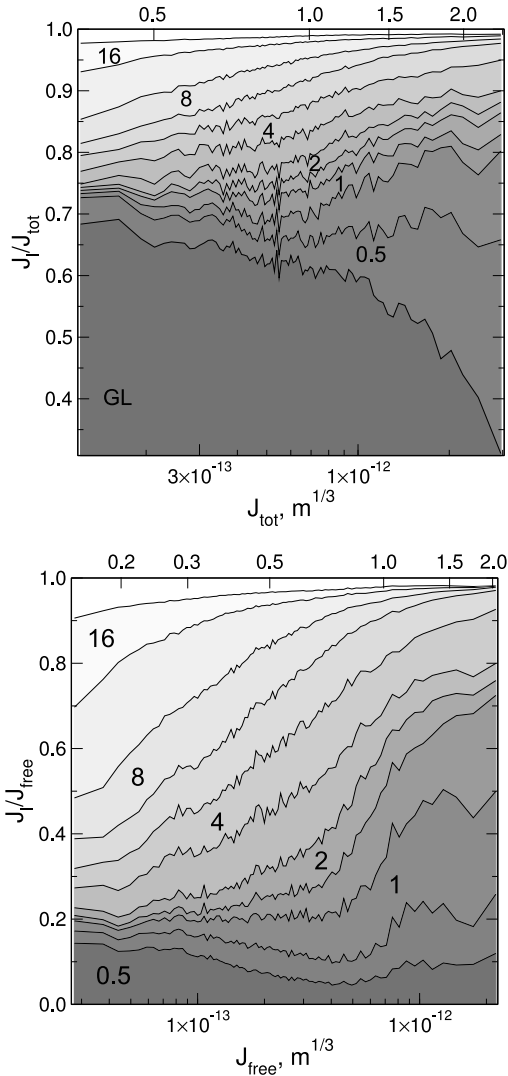


Figure 12. Structure of turbulent atmosphere as it depends on the total intensity J . The stripe thickness reflects its fraction of the total. Top: the whole atmosphere structure as a function of J_{total} (i.e. including GL). Bottom: the free atmosphere structure as a function of J_{free} . Alternative (upper) X-axes provide the seeing scale in arcseconds.

many summits (at Las Campanas observatory $f = 0.63$ as Thomas-Osip et al. (2008) quote) except for those good sites which have a very thin ground layer, e.g. $f = 0.46$ at Mauna Kea (Skidmore et al. 2009).

8.3 Structure of turbulent atmosphere

Many authors (e.g. see Tokovinin & Travouillon 2006) notice that the OT distribution character depends on the total intensity. In order to study the properties of the OT structure on the basis of the restored profiles, the median layer intensity fractions were plotted in Fig. 12 for the whole atmosphere and for the free one. Note that in these pictures a layer fraction is the *width* of the respective stripe.

In the top graph the full atmosphere structure is plotted against J_{total} . The abrupt lowering of the GL fraction above $J_{total} = 1 \cdot 10^{-12} \text{ m}^{1/3}$ is related to systematic effects in its

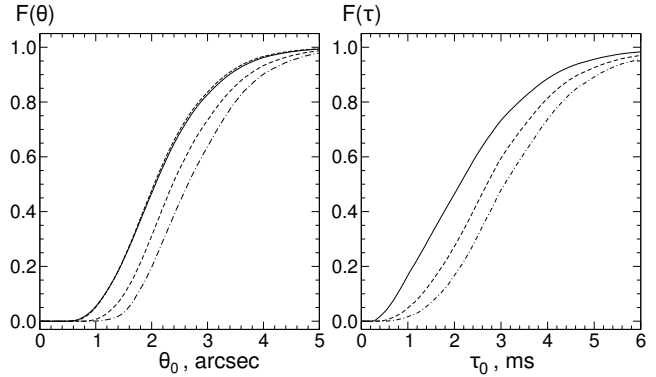


Figure 13. Left: integral isoplanatic angle θ_0 distributions for the whole data set (solid line), a $\beta_0 <$ median subset (dashed) and $\beta_0 < 25\%$ (dashed-dotted). The leftmost dashed line depicts θ_0 by OT profiles. Right: integral distributions of atmospheric constant τ_0 for the same data samples.

determination as discussed in the previous section. In the weaker turbulence domain the real diminishing of its fraction from 0.7 to 0.6 is seen. The sum intensity of the ground and 0.5-km layers accounts for about 0.70 of the total power in the whole J_{total} range.

It is informative that strengthening of the total turbulence is powered by the growth of lower 0.5 and 0.7 km layers which belong to the boundary region of atmosphere and also by the 4 and 6 km layers. This is accompanied by diminishing of the 8 to 16 km layers contribution which normally dominate when the total OT is weak. The increasing role of the lower layers may be ascribed to the thickening of the ground layer in bad conditions.

Changes in the free atmosphere structure as they evolve with its overall power are shown in the bottom plot of Fig. 12. The general tendency is an increase of the fraction of low layers with increasing total intensity of the OT in the free atmosphere. The whole range can be sub-divided in three domains: $\beta_{free} < 0.3 \text{ arcsec}$, $\beta_{free} > 1.0 \text{ arcsec}$ and an intermediate. The leftmost region corresponding to the best conditions shows the layers above 8 km dominating, in the intermediate conditions the major OT contribution descends to 2 – 8 km, and in the worst situation – down to 0.7 – 1.4 km.

8.4 Integral parameters

In addition to the OT profile restoration, the computed scintillation indices also serve for calculation of the altitude moments of turbulence as described in TKSv:

$$M_\alpha = \int C_n^2(h) h^\alpha dh \quad (10)$$

for $\alpha = 0, 1, 5/3, 2$. These moments are used for integral atmospheric parameters determination: free atmosphere seeing $\beta_{free}^{5/3} \sim M_0$, effective OT altitude $h_{eff} \sim M_1$, isoplanatic angle $\theta_0^{-5/3} \sim M_{5/3}$ and isokinetic angle $\theta_k^{-2} \sim M_2$. From the s_A^2 scintillation indices obtained with a tripled exposure the atmospheric coherence time τ_0 is estimated as proposed by Tokovinin (2002b). In these terms, the seeing β_0 obtained by the formula (5) is also a kind of integral parameter.

Table 6. Cumulative statistics of integral atmospheric parameters. Isoplanatic and isokinetic angles θ_0 and θ_k are in arcseconds.

	θ_0			θ_k		
	Q1	Q2	Q3	Q1	Q2	Q3
whole set	1.56	2.07	2.70	5.54	7.00	8.67
best 50% of β_0	1.88	2.38	3.06	6.42	7.78	9.52
best 25% of β_0	2.11	2.65	3.33	7.04	8.46	10.17

Table 7. Cumulative statistics of the time constant τ_0 , in ms.

	τ_0			τ_0 correct.		
	Q1	Q2	Q3	Q1	Q2	Q3
whole set	1.28	2.12	3.09	1.59	2.58	3.70
best 50% of β_0	1.92	2.70	3.67	2.40	3.34	4.46
best 25% of β_0	2.32	3.08	4.06	–	–	–

Atmospheric moments are computed as linear scintillation indices combinations where the related coefficients are derived from the needed h^α approximations by the weighting functions $Q(h)$ (TKSV). The feasible precision ($\delta < 0.05$) of this decomposition is attained at altitudes $h > 0.4$ km which is sufficient because lower layers produce almost no scintillation.

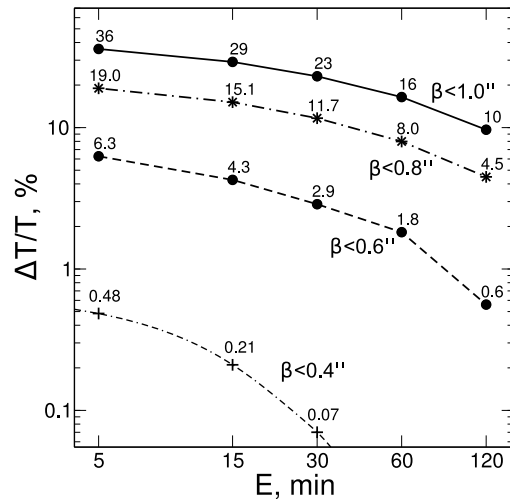
The isoplanatic angle determined from the $M_{5/3}$ agrees well with the angles computed from OT profiles. The regression slope is 0.98 with a rms scatter of 0.03 arcsec around it. The median θ_0 from profiles is 2.03 arcsec, differing by less than 2 percent from the θ_0 median calculated from the moments. This fact adds confidence to the results of OT restoration by the implemented algorithm.

Integral θ_0 distributions for three samples: the full scope of data, the cases of $\beta_0 < 0.93$ arcsec and of $\beta_0 < 0.73$ arcsec are shown in Fig. 13 (left) and their characteristics are listed in Table 6. Since θ_0 is essentially driven by turbulence in the upper atmosphere, its value is tied with the altitude of the summit. Given this circumstance, the obtained value is as good as at many other observatories.

For example, our MASS measurements at Maidanak (Kornilov et al. 2009) derived the characteristic θ_0 to be 2.19 arcsec which varied seasonally from 1.92 to 2.35 arcsec. Els et al. (2009) and Tokovinin & Travouillon (2006) list $\theta_0 = 1.56$ and 2.22 arcsec for Cerro Tololo and Cerro Pachon, respectively.

Values of the AO time constant τ_0 delivered by MASS and listed in Table 7 do not correspond to the standard definition of this quantity, as noticed by many authors. The estimates obtained by this method require a certain correction (see, for example, Travouillon et al. 2009). For correction of individual values, we used the formula (3) from the updated study of A.Tokovinin¹⁴. The statistics for corrected τ_0 are also shown in Table 7.

Isokinetic angle θ_k which provides the angular size of the wavefront slopes correlation has a special property to


Figure 14. Fraction of available continuous astronomical exposures of the duration E with a given limit of seeing β_0 .

depend not only on the wavelength but also on the telescope aperture. According to Hardy (1998) it relates to the turbulence second moment by the following expression:

$$\theta_k^{-2} = 0.688 \left(\frac{2\pi}{\lambda} \right)^2 D^{-1/3} M_2 \quad (11)$$

In Table 6 the characteristics of the observed θ_k distribution are given for the case of $\lambda = 500$ nm and the telescope $D = 2.5$ m. The comparison with the value derived from OT profiles shows a very good coincidence; the median isokinetic angle equals 7.01 arcsec. Explicit measurement of θ_k is omitted in a majority of site testing campaigns since it strongly correlates with the isoplanatic angle and depends (although weakly) on the aperture size.

9 DISCUSSION AND CONCLUSIONS

9.1 Results discussion

Detailed analysis and interpretation of the obtained results extend beyond the framework of the current study. Here we limit ourselves to two examples of the potential use of the provided information.

Various statistics of seeing and other relevant parameters are not sufficient for comprehensive characterization of the turbulent atmosphere properties at a given site. Of great importance are the temporal characteristics describing the typical rate of OT evolution, its time-scales of stability, and so on. These issues will be examined in forthcoming papers. In the current study we provide only a crude estimate of the temporal stability of seeing in a form suitable for a typical astronomical application.

In Fig. 14 we show the fractions of observing time suitable to deliver continuous periods E of the seeing better than a selected threshold. For example, the 30-minutes exposures with an image quality better than 0.6 arcsec are possible in 3 percent of the available observing time, which corresponds to 80 such exposures per year. If we restrict ourselves to 15-minutes exposures, we will get more than 230 frames per year. Such a statistic is evidently over-constrained, since short-term image deteriorations do not spoil the images that

¹⁴ <http://www.ctio.noao.edu/~atokovin/profiler/timeconstnew.pdf>

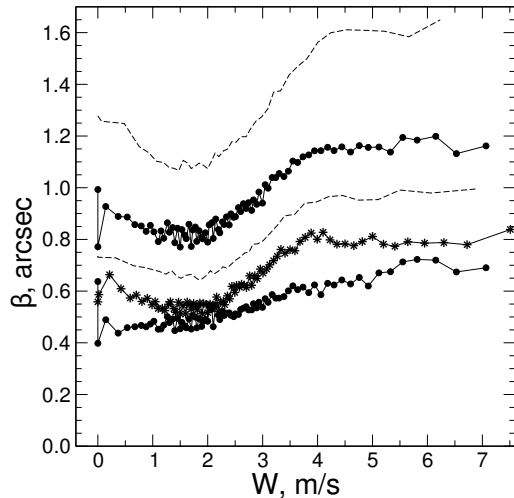


Figure 15. Dependence of the median seeing β_0 (black dots), β_{free} (open circles) and β_{GL} (stars) on the ground wind speed W . Dashed lines depict the first and third quartiles for β_0 .

seriously, but these ‘almost good’ exposures would not be counted. A similar prognosis of OT stability was presented in the paper of Travouillon et al. (2008).

Turbulence generation in the ground layer is usually related to mixing of local air masses by the wind. The characteristic feature of this phenomenon is the dependence of turbulence intensity on the ground wind speed. Such a correlation is observed at many sites, as reported by Thomas-Osip et al. (2008) and Skidmore et al. (2009). In Fig. 15 we plot the median seeing for the ground layer, free, and full atmosphere as a function of the recorded ground wind speed. These medians were calculated over groups of 1000 points. The effect is quite prominent, as reflected by the median values spread and interquartile range shown for β_0 .

It is also evident from the β_{GL} curve that strengthening of the ground wind causes first the decrease of the detected seeing which minimizes at speeds $1.5 - 2 \text{ m s}^{-1}$ and then starts getting worse with speeds up to 4 m s^{-1} . A similar effect is noted by Skidmore et al. (2009) at all monitored sites except San Pedro Martir. A further wind speed growth has already no effect on the ground turbulence but apparently increases the boundary layer seeing at 0.5 km and higher. It is remarkable that the minimum β_{GL} corresponds to the most probable wind speed at Shatdzhatmaz in clear night conditions, 2 m s^{-1} .

9.2 Conclusions

The measured basic site characteristics and OT profiles have confirmed the efficiency of the developed and built automatic site monitor. The OT data amount and quality exceed very significantly the results of our previous 3-year campaign performed at Mt. Maidanak in 2005 – 2007 in the manual observations mode (Kornilov et al. 2009). This convincingly justifies the time and resources invested in the complete automation of astronomical monitoring measurements.

Here we list the most significant site characteristics determined in the site testing program at Mt. Shatdzhatmaz in 2007 – 2009:

- The annual clear astronomical night time is 1343 hours, the clear nautical night time is 1546 h, under a rather strict clear sky criterion.
- The maximum of the clear sky amount is observed from mid-September to mid-March, where about 70 percent of the clear weather is concentrated.
- The mean clear night-time temperature is $+1.8^\circ\text{C}$, which implies a moderate water vapour content in the atmosphere.
- On clear nights, the median precipitable water vapour is 7.75 mm.
- The day-to-night temperature contrast is $\approx 3.4^\circ\text{C}$ for clear-sky weather.
- The median ground wind speed is 2.3 m s^{-1} with a preferred direction from the West.
- The median seeing β_0 is 0.93 arcsec. In 25 percent of time $\beta_0 < 0.73$ arcsec. The most probable seeing value is 0.82 arcsec.
- The free atmosphere median seeing β_{free} is 0.51 arcsec, the mode is 0.35 arcsec.
- The best seeing (minimal OT strength) is observed in October – November. The typical median value for that period is ≈ 0.83 arcsec.
- In conditions of the seeing better than a median one the optical turbulence is dominated by the ground layer, its fraction reaches 0.65.
- The periods of bad image quality occur when OT in the boundary and free atmosphere intensifies.
- The median isoplanatic angle is 2.07 arcsec in general and 2.38 arcsec in conditions of the seeing better than the median one.
- The median corrected atmospheric time constant is 2.58 ms, it exceeds 3.3 ms in conditions of weak turbulence.

These results are based on only two years monitoring and reflect the current situation at the site under evaluation. It is well known that the astroclimate parameters are subject of long-term trends and cycles, so the continued monitoring may introduce certain corrections. That is why we proceed further with the ASM operation. When the 2.5-m telescope will be put into operation at the observatory, the ASM functionality will be involved in the flexible observations planning.

The more extended site astronomical characterization demands also the monitoring of atmospheric extinction (also in the IR domain), of the sky background level and of such an important characteristic for AO as an altitude wind speed profile.

Nevertheless, it is already possible to characterize the potential of the studied summit as moderately high for astronomical observations. The basic parameters are slightly worse with respect to those of leading astronomical observatories, but not very significantly. The main conclusion is that modern methods of improving telescope resolution will be efficient at Shatdzhatmaz.

10 ACKNOWLEDGMENTS

The reported site testing and OT properties research at Mt. Shatdzhatmaz were performed under the partial support of the RFBR (grant 06-02-16902). Authors are grateful to the Pulkovo solar station staff, Sternberg institute colleagues

P. Kortunov, A. Belinsky, M. Kuznetsov and E. Gorbovskoy and students of the astronomical department of the Moscow University physical faculty for their help in the work. A special thank is to A. Tokovinin for numerous advices and discussions on the OT research problems throughout the project.

REFERENCES

- Avila R., Avilés J.L., Wilson R.W., Chun M., Butterley T., Carrasco E., 2008, *MNRAS*, 387, 1511
- Boshnjakovitch N.A., Bystrova N.V., Demidova A.N., Zhukova L.N., Kassinsky V.V., Eerme K.A., 1962, *Izvestiia GAO v Pulkove*, 22, Vyp (No) 5, 155
- Bowen, I. S., 1964, *AJ*, 69, 816
- Carrasco E., Avila R., Carramiñana A., 2005, *PASP*, 117, 104
- Darchiya A.H., Schmeel L.F., Darchiya S. P., 1960, *Izvestiia GAO v Pulkove*, 21, Vyp. (No) 6, 52
- Depenchuk E.A., Kondratyuk R.R., Kojfman A.P., 1977, in *Astrometr. Astrofiz.*, Vyp. (No.) 31, Naukova dumka, Kiev, p. 99
- Ehgamberdiev S. A., Baijumanov A. K., Ilyasov S. P., et al., 2000, *A&A Suppl.*, 145, 293
- Els S.G., Schöck M., Bustos E., Seguel J., Vasquez J., Walker D., Riddle R., Skidmore W., Travouillon T., Vogiatzis K., 2009, *PASP*, 121, 922
- Fuchs A., Tallon M., Vernin J., 1998, *PASP*, 110, 86
- Fuensalida J., Chueca S., Delgado J.M. et al, 2004, in *Ardeberg A.L., Andersen T., eds, Second Backaskog Workshop on Extremely Large Telescopes*, Proc. SPIE 5382, p. 619
- Gnevysheva K.G., 1991, *Izvestiia GAO v Pulkove*, 207, 77
- Hardy J.W., 1998, *Adaptive Optics for Astronomical Telescopes*, Oxford University Press
- Kornilov V., Kornilov M., 2010, preprint (arXiv:1005.4658v1 [astro-ph.IM])
- Kornilov V., Tokovinin A., Voziakova O., Zaitsev A., Shatsky N., Potanin S., Sarazin M., 2003, in *Wizinovich P.L., Bonaccini D., eds, Adaptive Optical System Technologies II*. Proc. SPIE 4839, p. 837
- Kornilov V., Tokovinin A., Shatsky N., Voziakova O., Potanin S., Safonov B., 2007, *MNRAS*, 382, 1268
- Kornilov V., Ilyasov S., Vozyakova O., Tillaev Yu., Safonov B., Ibragimov M., Shatsky N., Egamberdiev Sh., 2009, *Astronomy Letters*, 35, 547
- Leushin V.V., Nelyubin N.F., Nebelitskij V.B., Novikov S.B. 1975, *Astron. Tsirk*, No. 866, 6
- Lipunov V., Kornilov V., Gorbovskoy E., Shatskij N. et al., 2010, *Advances in Astronomy*, 2010, 1
- Martin H.M., 1987, *PASP*, 99, 1360
- Nelyubin N.F., Vasilyev O. B., 1969 *Astrofiz. Issled. Izv. Spets. Astrofiz. Obs.*, 1, 185
- Riddle R., Schoeck M., Skidmore W., 2006, in *Stepp L., ed., Ground-based and Airborne Telescopes*, Proc. SPIE 6267, p. 1Q
- Roddier F., 1981, in *Wolf E., ed., Progress in Optics*, 19, North-Holland, Amsterdam, p. 281
- Roddier F., 1999, *Adaptive optics in astronomy* Cambridge, Cambridge Univ. Press, New York
- Rylkov V.P., Bobilev V.V., 1991, *Izvestiia GAO v Pulkove*, 207, 89
- Sarazin M., Roddier F., 1990, *A&A*, 227, 294
- Saunders W., Lawrence J., Storey J. et al, 2009, *PASP*, 121, 976
- Schoeck M., Els S., Riddle R. et al., 2009, *PASP*, 121, 384
- Skidmore W., Els S., Travouillon T., Riddle R., Schöck M., Bustos E., Seguel J., Walker D., 2009, *PASP*, 121, 1151
- Soules D.B., Drexler J.J., Draayer B.F., Eaton F.D., Hines J.R., 1996, *PASP*, 108, 817
- Tatarskii V.I., 1967, *Wave Propagation in a Turbulent Medium*. Dover Press, New York
- Tokovinin A., 2002a, *PASP*, 114, 1156
- Tokovinin A., 2002b, *Appl. Opt.*, 41, 957
- Tokovinin A., Baumont, S., Vasquez J., 2003, *MNRAS*, 340, 52
- Tokovinin A., Kornilov V., 2007, *MNRAS*, 381, 1179
- Tokovinin A., Sarazin M., Smette A., 2007, *MNRAS*, 378, 701
- Tokovinin A., Travouillon T., 2006, *MNRAS*, 365, 1235
- Tokovinin A., Kornilov V., Shatsky N., Voziakova O., 2003, *MNRAS*, 343, 891 (TKSV)
- Tokovinin A., Bustos E., Berdja A., 2010, *MNRAS*, 404, 1186
- Thomas-Osip J. E., Prieto G., Johns M., Phillips M.M., 2008, in *Stepp L.M., Gilmozzi R., eds, Ground-based and Airborne Telescopes II*, Proc. SPIE 7012, p. 1U
- Thomsen M., Britton M., Pickles A., 2007, *BAAS*, 38, 242
- Travouillon T., Els S.G., Riddle R.L., et al., 2008, in *Stepp L.M., Gilmozzi R., eds, Ground-based and Airborne Telescopes II*, Proc. SPIE 7012, 20
- Travouillon T., Els S., Riddle R. L., Schöck M., Skidmore W., 2009, *PASP*, 121, 787
- Vernin J., Caccia J.-L., Weigelt G., Mueller M., 1991, *A&A*, 243, 553
- Vernin J., Muñoz-Tuñon C., Sarazin M., 2008, in *L. Stepp, R. Gilmozzi, eds, Ground-based and Airborne Telescopes II*, Proc. SPIE 7012, p. 1T
- Wilson R.W., 2002, *MNRAS*, 337, 103
- Wilson R. W., Wooder N.J., Rigal F., Dainty J. C., 2003, *MNRAS*, 339, 491
- Wilson R., Butterley T., Sarazin M., 2009, *MNRAS*, 399, 2129